A Quasi-Monte Carlo method to compute scattering effects in radiative heat transfer: Application to a sooted jet flame

Kevin Torres Monclard, Olivier Gicquel, Ronan Vicquelin

A Quasi-Monte Carlo method to compute scattering effects in radiative heat transfer: application to a sooted jet flame

K. Torres-Monclard[a,*], O. Gicquel Olivier[a], R. Vicquelin[a]

[a] *Laboratoire EM2C, CNRS, CentraleSupélec, Université Paris-Saclay, 8-10 rue Joliot Curie, 91192, Gif-sur-Yvette cedex, France*

Abstract

The Monte-Carlo simulation of radiative heat transfer is known to be very accurate. Its convergence can be significantly improved using Randomized Quasi-Monte-Carlo (RQMC) methods that rely on low-discrepancy sequences. The RQMC approach derived recently to deal with thermal radiation is, however, limited to non-scattering media. The present work proposes a methodology aiming at extending this technique to scattering media based on the prior estimation of the low-discrepancy sequence dimension. Firstly, the method is tested on 3D homogeneous fields with various operating points based on the domain's optical thickness and albedo. It is observed that, for a given number of generated rays, the error can be reduced by up to one order of magnitude. Secondly, the RQMC approach is combined with importance sampling to increase its efficiency further. The number of rays required is even lower, resulting in saving CPU time to reach a given error.

The RQMC approach is then applied along with an accurate model for soot particles' radiative properties: the Rayleigh-Debye-Gans for Fractal Aggregates (RDGFA) theory. The model assumes a complex morphological shape of particles contrary to Rayleigh theory that is valid for spherical particles only. Monte-Carlo simulations are performed on a fixed turbulent sooted flame field taken from coupled calculations with large-eddy simulation. The overall CPU cost

*Corresponding author : kevin.torres-monclard@centralesupelec.fr

is divided by a factor of 2 compared to a standard Monte Carlo calculation. The simulation allows for accurate quantification of soot scattering effects with RDGFA, which eventually appear small in this configuration. On the other hand, the use of Rayleigh theory strongly underpredicts the actual scattering impact.

Keywords: Thermal radiation, Monte Carlo, Soot, Scattering

1. Introduction

The radiative contribution to wall fluxes must be determined in many engineering systems, particularly in combustion chambers which feature high temperatures. In such applications, radiative heat transfer is classically split into two contributions: non-luminous radiation from participating burnt gases on the one hand, and luminous radiation from soot particles emitted in the visible spectral range on the other hand. It is known the latter is contributing to a non-negligible part of the wall fluxes in gas turbines [1]. Hence, radiative heat transfer from soot particles must be understood and quantified.

The characterization of soot radiative properties from their morphology has shown an increasing interest [2–5] since these properties have an impact on the radiative transfer properties [6–8], but also on soot growth mechanisms. Soot particles are known to form aggregates of n_P primary particles with quasi constant primary particle diameter d_P. In practice, such a complex geometry is considered as a fractal structure. Although their shape varies irregularly, empirical laws have been proposed to describe these clusters. The law of Samson [9] expresses the relationship between n_P and d_P as $n_P = k_f \left(\frac{2R_g}{d_P}\right)^{D_f}$ with k_f and D_f fractal parameters.

Several experimental diagnostics have been developed for soot characterization on laminar flames. The LII (Laser-Induced Incandescence) enables access to the soot volume fraction f_V [10, 11] , but this technique needs to be calibrated and depends on the optical properties of soot particles. The determination of n_P and d_P are based on experimental diagnostics such as the Laser Light Extinction

techniques based on the scattering by soot particles [12, 13].

From a numerical point of view, the computation of the radiative power is based on solving the Radiative Transfer Equation (RTE) accounting emission, absorption, and scattering phenomena. Among the different existing methods [14], the Discrete Ordinate Method (DOM), Finite Volume Method (FVM), and Monte Carlo (MC) methods are the most popular. The latter is known to be the most accurate and is used as a reference for the other methods, although it is computationally expensive. Numerous studies have been focusing on radiation impact, using detailed radiative properties for gaseous combustion products (line-by-line method or a narrow-band approach such as the cK-model [15]) with both RANS and LES approaches [16–19]. Taking into account soot particle radiation requires additional modeling effort since their optical properties, morphology, and dynamics need to be described accurately. Although state-of-the-art soot dynamics model has been considered in some studies (method of moments: [20]; sectional method: [21]) along with a Monte Carlo resolution, scattering by soot particles, have always been neglected. This is due to the use of Rayleigh theory to describe soot particles' radiative properties in CFD computations: in this theory, soot particles are considered as spherical and small, and scattering is negligible. However, more recent approaches, as the Rayleigh-Debye-Gans theory for Fractal Aggregates (RDG-FA) [22], have been developed and consider soot particles as fractal aggregates. This is more consistent with experimental findings. Recent work [23] has also compared RDGFA results with exact solutions for a cluster of spheres and has shown the excellent capability of RDGFA to describe complex scattering interactions between primary particles. The effects of soot scattering based on Rayleigh theory could then have been wrongly estimated in previous CFD studies and should be quantified with up-to-date models such as RDGFA.

Combining scattering and Monte Carlo resolution is done in other research fields such as stellar observation [24–26] or medical approaches [27]. In these studies, several techniques of Monte Carlo convergence improvements have been employed since the variance due to the scattering was important. One of these

techniques is known as the Forced Scattering [25] and are using the idea of biasing: the random numbers are generated from a probability density function (PDF) $q(x)$ instead of the original one $p(x)$. The weight of the Monte Carlo ray is then corrected by a factor $1/q(x)$. This enables to reduce the variance of the Monte Carlo estimate and then have a better estimation of the radiative power or flux. However, since a Monte Carlo cubature method is used, the convergence rate law is known to be proportional to $N^{-1/2}$ with N the total number of rays, which can keep the calculations costly.

High-fidelity simulations of turbulent reactive flows with a Monte Carlo method and detailed soot radiative properties, including scattering, have never been done before. It would remain, however, very costly if the scattering effects to outline are small. Additional efforts are needed to make such computations more affordable. Several strategies can be encountered in the literature. When the origin of penalized convergence is identified, variance reduction techniques [28–31], which Forced scattering is a part of, are of great interest. Recently, an alternative sampling mechanism for numerical integration known as Quasi-Monte Carlo (QMC) has been applied to radiative energy transfer in participating media [32, 33]. Such a methodology, which can be combined with any other variance reduction techniques, improves the convergence rate of the Monte Carlo simulation significantly. In particular, [32] have used a Randomized QMC (RQMC) that enables the statistical estimation of the results accuracy and have demonstrated its increased efficiency in several cases. RQMC simulations of thermal radiation have been retained in recent coupled simulations: direct numerical simulation of a turbulent jet [34] and large-eddy simulation of a sooted jet flame [21].

The purpose of this study is twofold. A Randomized Quasi-Monte Carlo methodology is first derived to handle scattering media and extend the range of radiative transfer applications for such interesting methods. It is combined with different scattering treatment strategies, and the impact on the simulations' accuracy and convergence rate is analyzed. Secondly, the derived approach is applied to a 3D simulation of a turbulent sooted jet flame to quantify soot

scattering with state-of-the-art soot radiative models (RDG-FA). The flame corresponds to the one experimentally studied at Sandia [35], and the radiative fields are computed from large-eddy simulation instantaneous results extracted from [21].

The study is organized as follows: Section 2 introduces the Monte Carlo solver, the implemented standard methods to deal with scattering, and the adaptation of RQMC in this context. The validation of these methods and their impact on convergence are shown in Section 3. Sections 2-3 involve gray properties and a homogeneous domain. Soot radiative properties used to compute the radiative power of the turbulent jet flame are presented in Sec. 4. The Rayleigh-Debye-Gans theory for Fractal Aggregates is fully detailed with the retained parameters and validated. Finally, Section 5 presents the different results obtained in this turbulent configuration. The benefit of the RQMC method in CPU time and error is first evaluated. The reference fields computed without scattering are then presented along with the impact of soot particles scattering.

2. Monte Carlo resolution of the RTE with scattering.

2.1. The Rainier solver

2.1.1. Radiative transfer equation

In this study, the Radiative Transfer Equation (RTE) is solved for a participating medium, accounting for emission, absorption and scattering effects. In these conditions, the RTE is given by :

$$\frac{\mathrm{d}I_\nu}{\mathrm{d}s} = -\left(\kappa_\nu + \sigma_\nu\right) I_\nu + \kappa_\nu n^2 I_{b\nu} + \frac{\sigma_\nu}{4\pi}\int_{4\pi} I_\nu(\mathbf{s}')\Phi_\nu(\mathbf{s}',\mathbf{s})\mathrm{d}\Omega' \tag{1}$$

In this equation, the radiative intensity I_ν is a function of the local position, the direction $\mathbf{s}$ and the wavenumber ν. The refractive index of the medium n is considered as unity in the following. κ_ν and σ_ν are the absorption and scattering coefficients, respectively. $I_{b\nu}$ is the blackbody intensity and $\mathrm{d}\Omega'$ the infinitesimal solid angle around the direction $\mathbf{s}'$. The first term of the equation corresponds to a loss of radiative intensity in the direction $\mathbf{s}$ due to absorption and scattering.

The second term accounts for the emission process. The last term represents the fraction of intensity coming from another direction $\mathbf{s}'$ scattered in the direction $\mathbf{s}$. This fraction depends on the scattering phase function $\Phi_\nu(\mathbf{s}', \mathbf{s})$, which can be seen as the probability for a ray to be scattered from $\mathbf{s}'$ to $\mathbf{s}$.

2.1.2. Monte Carlo solver

The Radiative Transfer Equation (RTE) is solved with a Monte Carlo approach using the in-house code Rainier [32] whose details are summarized here. In this solver, a backward Monte Carlo method, the Emission Based Reciprocity Method (ERM), [36] is used to compute the radiative power and flux fields. In ERM, the radiative power at a given node is calculated as the sum of the exchanged power with all other cells and the computational domain's boundary faces. The exchanged power between the node i and the cell j is given by:

$$P_{ij}^{\text{exch}} = \int_{\nu=0}^{+\infty} \kappa_\nu\left(T_i\right)\left[I_{b\nu}\left(T_j\right) - I_{b\nu}\left(T_i\right)\right] \int_{4\pi} A_{ij\nu} d\Omega d\nu \tag{2}$$

T_i and T_j are the temperature at the node i and cell j, respectively. The term $A_{ij\nu}$ accounts for absorption, transmission, and wall reflections between i and j.

In the Rainier solver, rays are traced from all the computational domain nodes where a result is desired. The ray is characterized by its initial position (same as a node of interest), its wavenumber ν, and its initial direction (corresponding to two angles θ and ϕ). The three latter quantities are randomly sampled according to their probability density functions, and associated with three random numbers R_ν, R_θ and R_ϕ uniformly sampled between zero and unity:

$$R_\nu = \frac{\int_0^\nu \kappa_\nu\left(T_i\right) I_{b\nu}\left(T_i\right) d\nu}{\int_0^\infty \kappa_\nu\left(T_i\right) I_{b\nu}\left(T_i\right) d\nu}, \quad R_\theta = \frac{1-\cos(\theta)}{2}, \quad R_\phi = \frac{\phi}{2\pi}. \tag{3}$$

For black walls or specular reflection, no additional random numbers are needed. In the case of diffuse reflections, the reflected direction needs to be randomly generated, and two new random numbers R'_θ and R'_ϕ are sampled in the corresponding hemisphere.

The path that the ray follows is treated with the energy partitioning method or path-length method [37]. The ray is gradually attenuated along its path by a factor $e^{-\kappa \Delta l}$ after each cell's crossing, where Δl is the path length through one cell, and after each wall reflection. A stopping criterion is given in practice: the bundle is traced until it carries a certain percentage of its initial energy τ_{min}.

2.1.3. Accuracy monitoring

Finally, to estimate the Monte Carlo simulations' error, the total number of ray samples N is divided into M packs, yielding M sub trials. For a given pack i, the Monte Carlo trial $Q_i(P)$ is computed, with $P = N/M$ the number of rays in the pack. The Monte Carlo estimate from the total number of rays $Q_(N)$ is then given by :

$$Q(N) = \frac{1}{M} \sum_{i=1}^{M} Q_i(P) \tag{4}$$

In practice, Q designates either the radiative power or the radiative flux. The knowledge of $Q(N)$ and $Q_i(P)$ enables to estimate the standard deviation of $Q(N)$ as

$$\sigma[Q(N)] \approx \left(\frac{1}{M(M-1)} \sum_{i=1}^{M} [Q_i(P) - Q(N)]^2 \right)^{1/2} \tag{5}$$

The accuracy of the Monte Carlo results is controlled thanks to two convergence criteria based on the standard deviation $\sigma[Q(N)]$:

- Relative error: it is defined as the ratio of the local standard deviation to the local quantity of interest (radiative power or flux).
- Absolute error: the standard deviation is checked to be lower than a prescribed threshold, typically set equal to a given percentage of the estimated maximum value of the quantity of interest.

Once one of these criteria is attained, the ray tracing is interrupted.

2.2. Standard stochastic treatment of scattering

The Rainier solver did not account for scattering in previous works. The implemented stochastic treatment of scattering combined with energy partitioning for absorption and ERM follows the Ph.D. work of Tessé [38]. The method does not modify the radiative power expression, and scattering events only correspond to a modification of the ray's direction.

2.2.1. Optical thickness for scattering

In the Monte Carlo method, each ray follows the standard ERM until a given distance determined by the attributed scattering optical thickness is reached. A scattering event is then computed. The optical thickness (for scattering) of each ray is based on a random number sampled uniformly between 0 to 1 that corresponds to a value of a cumulative probability distribution function (*c-pdf*). The scattering *pdf*, indicating the probability that a a ray changes its direction between s and $s + \mathrm{d}s$, is equal to :

$$f_s(s)ds = \exp\left[-\int_0^s \sigma_\nu\left(s'\right)\mathrm{d}s'\right]\sigma_\nu \mathrm{d}s \tag{6}$$

Then, the cumulative probability function (*c-pdf*) F_s is defined by :

$$F_s(s) = \int_0^s f_s(s')\mathrm{d}s' = 1 - \exp\left[-\int_0^s \sigma_\nu\left(s'\right)\mathrm{d}s'\right] \tag{7}$$

One can define an optical thickness for scattering $\tau_s = \int_0^s \sigma_\nu\left(s'\right)\mathrm{d}s'$, and a random number R_s (corresponding again to a value of F_s) given by :

$$\tau_s = -\ln(R_s) \tag{8}$$

2.2.2. Scattering event

Determination of the scattering location.

Let N_c be the number of cells crossed by the ray, and l_i the length crossed by the ray in the i-th cell. The scattering event occurs in the cell N_c if $\sum_{i=0}^{N_c} \sigma_{i,\nu} l_i > \tau_s$.

The length l_s from the cell entry point at which the scattering takes place is determined by

$$l_s = \frac{\sum_{i=1}^{N_c} \sigma_{i,\nu} l_i - \tau_s}{\sigma_{N,\nu}} \tag{9}$$

The radiative power exchanged between the ray origin and the cell N_c is calculated using the distance l_s.

Determination of the new direction.

At this point, the new direction is unknown and needs to be determined. The scattered ray is parametrized by two new angles θ_s and ϕ_s defined in respect to the ray direction. Two new random numbers R_θ and R_ϕ are sampled accordingly. Their definition depends on the scattering phase function Φ. In this study, isotropic scattering and the RDG-FA model for soot particles are considered.

- Isotropic scattering

$$\begin{aligned} \phi_s &= 2\pi R_\phi \\ \cos(\theta_s) &= 1 - 2R_\theta \end{aligned} \tag{10}$$

- Anisotropic scattering with RDG-FA. Φ is only a function of θ (cf. Equation 25).

$$\begin{aligned} \phi_s &= 2\pi R_\phi \\ R_\theta &= \frac{\int_0^{\theta_s} \Phi(\theta) \sin(\theta)\, \mathrm{d}\theta}{2} \end{aligned} \tag{11}$$

Once the new direction is known, a new scattering optical thickness is sampled, and the ray tracing continues.

2.3. Improvement of the methodology with forced-scattering

One issue with this standard methodology is that the scattering criterion $\sum_{i=0}^{N} \sigma_{i,\nu} l_i > \tau_s$ can be rarely verified in areas with a low scattering optical thickness. Consequently, to achieve a statistically significant number of scattering

events in these regions, a considerable number of sampling would be required, leading to an increase in CPU cost.

The idea of forced-scattering [25] is to limit the value taken by τ_s to guarantee that a ray is scattered along its path. Equation 8 is then modified and becomes

$$\tau_s = -\ln(R_s(1 - e^{\tau^*})) \tag{12}$$

with τ^* the total optical depth along a ray's path from the emitted point to a wall of the domain. Since the physics has been biased, the exchanged power after scattering is corrected accordingly by a factor $\frac{1}{1-e^{\tau^*}}$.

The quantity τ^* is pre-computed at the point of emission before the usual ray tracing begins to determine the radiative power or flux. After the initial direction is randomly generated, the quantity $\tau^* = \sum_{i=0}^{N} \sigma_{i,\nu} l_i$ is calculated until the ray reaches a wall. Although this technique improves convergence, it increases the CPU cost due to this additional ray generation.

To overcome this difficulty, an approximation of the quantity τ^* is done, by prescribing $\tau^*_{fast} \approx \sigma_{emit,\nu} L_{max}$ where L_{max} is a quantity explicitly chosen before any computation. In practice, it is set to be equal to the maximum length of the domain. $\sigma_{emit,\nu}$ corresponds to the scattering coefficient's value at the emission point. This technique will be referred to as *fast forced-scattering* method in the following.

Once a ray is scattered, a new random optical thickness is computed as explained in the previous part. In this case, the above procedure is repeated by computing τ^* or τ^*_{fast} from the scattering point.

2.4. Randomized Quasi-Monte Carlo treatment of scattering

2.4.1. Quasi-Monte Carlo

The Quasi-Monte Carlo (QMC) methodology has been implemented and validated in the Rainier solver [32] for a non-scattering medium. The QMC technique relies on the use of low-discrepancy sequences instead of the usual random number generators. This enables to improve the rate of convergence of the iterative method. The construction of the low-discrepancy sequence requires

to know beforehand the stochastic dimension of the problem. The stochastic dimension corresponds here to the number of different random variables to initialize and trace a ray. This construction requirement is fundamentally different from the classical use of a single random generator that provides (with a given quality) independent and identically distributed (i.i.d.) samples for all needed random variables. In this work, a Sobol sequence is used. Its construction algorithm follows the algorithm described in [39]. The stochastic dimension, *i.e.* the number of different random variables, is in the general unknown in Monte Carlo simulations addressing radiative heat transfer. This issue is common to all QMC methods and has not been studied in scattering media.

2.4.2. Stochastic dimension and scattering

For a non-scattering medium with diffuse wall reflections, the sequence dimension is here equal to $d = 3+2r_{max}$. The number 3 corresponds to the initial random numbers picked up for the ray (wavenumber ν, direction angles θ and ϕ). r_{max} is the maximum number of diffuse reflections of a ray which can be determined as a function of the wall properties [32]: $\frac{\ln(\tau_{\min})}{\ln(1-\epsilon_{\min})}$ where τ_{min} and ϵ_{min} are the stopping ray criterion and the minimal wall emissivity encountered in the simulation, respectively. Finally, for each reflection, 2 random numbers are sampled to define the reflected direction.

In the case of a scattering medium, determining beforehand the number of scattering events of a ray is problematic or, at best, cumbersome: the different fields (temperature, species, soot) are not homogeneous, and time-varying in coupled simulations involving DNS or LES. However, this knowledge is required before any computation to build the corresponding low-discrepancy sequence. Let us denote s_{max} the prescribed maximum number of scattering events for a ray. The dimension of the sequence is then equal to $4 + 2r_{max} + 3s_{max}$ when accounting for scattering. Four random variables are now needed at the beginning of the computation with the added scattering optical thickness to sample. After each scattering event, three random numbers are sampled.

Since the user choice of s_{max} could be underestimated, one can run out of samples in the QMC sequence. Two strategies are then considered to deal with scattering:

- *Hybrid-RQMC* method: QMC samples are considered for emission and wall reflections only ($d_{QMC} = 3 + 2r_{max}$); scattering is fully treated with a standard Monte Carlo approach.
- *Full-RQMC* method: the QMC method is used for emission, wall reflections and scattering up to s_{max} events ($d_{QMC} = 4 + 2r_{max} + 3s_{max}$); when s_{max} is reached, additional sampling switches to a standard random generator, *i.e* a Monte Carlo method instead of QMC.

The RQMC concept, which extends the QMC method, is introduced below. In the first strategy (*Hybrid-RQMC*), QMC only benefits to the first part of the rays tracing where the stochastic dimension is known with certainty. In the second strategy (*Full-RQMC*), QMC sampling is used up to the initial fixed full stochastic dimension. Beyond s_{max}, we choose not to interrupt the ray tracing to bias the computed results, and the solver relies then on a standard MC sampling.

2.4.3. Accuracy monitoring with randomized QMC

Compared to Monte Carlo simulations and the associated central limit theorem, the QMC method uses a deterministic sequence whose points are no longer independent. Consequently, QMC does not provide a way to estimate the error, which prevents any computations' accuracy control. Such an issue can be solved by randomizing the low-discrepancy sequences [40], known as the Randomized QMC (or RQMC) approach.

In this approach, M trials of low-discrepancy sequences are built, each composed of P realizations. Each sequence is a randomized version of the original low-discrepancy sequence, which ensures independence between them. This en-

ables, following equations 4 and 5 to have access to the standard deviation of the RQMC estimator of our quantity of interest, by :

$$\sigma\left[Q^{\mathrm{RQMC}}(N)\right]^2 \approx \frac{1}{M(M-1)} \sum_{i=1}^{M} \left[Q_i^{\mathrm{QMC}}(P) - Q^{\mathrm{RQMC}}(N)\right]^2 \qquad (13)$$

where $N = M\,P$ is the total number of realizations, $Q^{\mathrm{RQMC}}(N) = \frac{1}{M}\sum_{i=1}^{M} Q_i^{\mathrm{QMC}}(P)$ is the RQMC estimator of the quantity of interest. When considering Quasi-Monte Carlo simulations in the following, only RQMC computations are actually carried out. RQMC computations are of great interest in practical simulations where on-the-fly control of the accuracy is desired. Finally, the different methods' convergence rates can be quantified identically based on the evolution of the estimate's standard deviation with the total number of samples N.

To build a randomized QMC sequence, a balance must be found between the resulting scrambling of the samples and the need to preserve the low-discrepancy property, which makes the QMC cubature efficient in the first place. The I-binomial scrambling method [41] has been retained in this study: it preserves the convergence results of the interesting Full Scrambling method while ensuring a good compromise between memory requirement and computational cost. The key principle is the application of a permutation to each digit issued from the decomposition of the sequence points in base b (b = 2 for the considered Sobol sequence). The I-binomial scrambling is part of the linear scrambling techniques, where the permutations are constructed through linear combinations. More details on the construction algorithm can be found in Refs.[41, 42].

3. Validation and assessment of convergence properties in a homogeneous gray medium

3.1. Test case

All the calculations carried out in this section assume uniform gray radiative properties and isotropic scattering. Other validation cases encountered in the literature have mostly been realized in these conditions.

The chosen validation case is taken from the study of [43]. A 1D domain with a uniform temperature of 1000 K and gray radiative properties is considered. Two black walls at 300 K surround the domain. The medium is characterized by an extinction optical thickness $\tau_L = (\kappa + \sigma)L$ with L the domain length, and an albedo $\omega = \frac{\sigma}{\kappa+\sigma}$. Knowing these two quantities, the radiative properties of the medium are completely described by $\sigma = \frac{\omega \tau_L}{L}$ and $\kappa = \frac{\tau_L}{L} - \sigma$.

The wall emittance is defined as the ratio $\frac{\varphi_r}{\varphi_{black}}$ with φ_r the wall radiative heat flux and φ_{black} the corresponding black body wall flux at the given wall temperature. Siegel [43] has reported emittance values that validate the current implementation of scattering in the Rainier solver.

3.2. Validation of the standard scattering treatment

The standard Monte Carlo treatment of scattering described in Sec. 2.2 and added in the Rainier solver is here assessed on a 3D cubic domain $L_x \times L_y \times L_z$ with $L_x = L_y = L_z = 0.2$ m. The x-axis corresponds to the wall-normal direction. The domain is discretized on a structured mesh: $N_x = 100$, $N_y = 100$, $N_z = 10$. The MC backward method enables the computation of the points of interest located at the left and right walls. Periodic boundaries are applied to the four other walls.

The error control is set such that the relative error on the computed flux is 1%. Since the error is fixed here, the number of rays is allowed to vary until the error is reached. For this validation case, the number of packs M is set to 100. Scattering is here treated with the *Hybrid-RQMC method*. The results obtained with the Rainier solver are compared with the study of Siegel in Figure 1.

It can be observed that the amount of heat flux impinging the wall diminishes as the albedo increases. Indeed, the medium scatters more energy, which, after absorption, does not reach the wall. When the total optical thickness increases, the normalized heat flux increases because the medium emits more energy. The obtained results are in excellent agreement with Siegel's work, which validates the implemented methodology to deal with a scattering in the radiation solver.

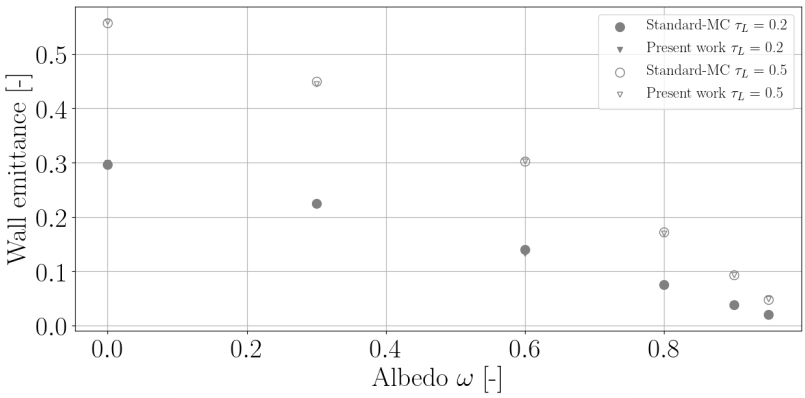

Figure 1: Wall emittance obtained in function of the albedo ω for two optical thickness τ_L and comparison with literature data [43]. (higher resolution)

3.3. Comparison of different methods

In the previous section, a controlled error has been prescribed. The objective of this section is to apply several techniques to compare the convergence of the calculations. The CPU time is directly related to the number of rays required to achieve the prescribed accuracy.

3.3.1. Validation

The following methods are considered:

- The *hybrid-RQMC* case used for the validation of standard scattering in Section 3.2 (RQMC for absorption and emission, MC for the scattering)
- The *Standard forced-scattering* (SFS) case. In order to assess the validity of the method, absorption, emission and scattering are treated with a standard MC approach.
- The *Fast-forced-scattering* (FFS) case, with a maximum length is prescribed to $L_{max} = 0.2$ m, which corresponds to the size of the domain. A classical MC approach is also used here for the random number generation.

- The *full-RQMC* case where scattering is also treated using RQMC. For this computation, a value of $s_{max} = 50$ is chosen in order not to affect the obtained results. This choice yields a Sobol sequence dimension of 154.

The number of trials M is set to 100, and the same convergence criteria are prescribed to all cases for the absolute and relative standard deviation. The obtained results are shown in Figure 2. The different methodologies give identical results, which is expected with the controlled error. This validates their implementation.

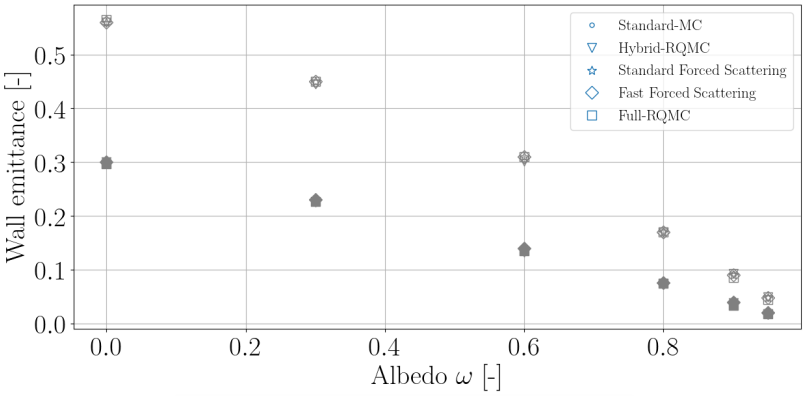

Figure 2: Wall emittances obtained in function of the albedo ω for two optical thickness τ_L and for four different scattering treatments. Comparison with reference results from [43] is also provided. Plain markers : $\tau_L = 0.2$, empty markers : $\tau_L = 0.5$.

3.3.2. Convergence performance : tests with fixed number of rays

In the previous section, the number of rays was allowed to vary since an error criterion was prescribed. The different methods do not take the same computational time. Additional computations are performed by calculating the error of all the methods for a fixed number of rays to assess the improved methods' convergence performance. The error is assessed with each method's standard deviation for their estimation of the wall radiative flux.

The case with optical thickness $\tau_L = 0.2$ and albedo $\omega = 0.3$ is first considered. The four methods compared in Section 3.3.1 are considered. The number

of trials M is fixed at 100 for a correct estimation of the standard deviation. $s_{max} = 50$ is set for the *full-RQMC* computation. An additional method where emission, absorption, and scattering (standard treatment) are all treated via a traditional Monte Carlo approach is also exhibited for reference. This method is referred to as *Standard-MC*.

In Figure 3, the methods exhibit different curves of relative standard deviation as a function of the total number of rays N. For larges values of N, the asymptotic convergence law is outlined. Three trends can be observed in Figure 3. For the cases with a standard Monte Carlo treatment, *Standard-MC, SFS* and *FFS* cases, the classical $N^{-1/2}$ convergence law of MC methods is retrieved. One can note that the errors achieved for these cases are similar here. This is attributed to the chosen conditions (optical thickness and albedo) where scattering is not dominant: *SFS* and *FFS* do not increase the convergence in this case. When a *full-RQMC* treatment is considered, the convergence rate is greatly improved (up to 0.8), and the lowest error is obtained with this method. Typically, if one requires a relative standard deviation of 10^{-3}, approximatively 10^4 rays need to be computed for the RQMC method, while 10^5 rays are required for the standard MC method, which saves an important CPU time. The difference increases as the desired error are lowered. With a hybrid-approach (*Hybrid-RQMC*), the error and corresponding convergence law are in-between the *Standard-MC* and *full-RQMC* cases. The power-law exponent is slightly affected here by the standard MC treatment of scattering, limiting the achieved error.

A second case with $\tau_L = 1$ and the albedo $\omega = 0.7$ is considered to see how the previous results are affected. The number of maximum scattering has been increased to $s_{max} = 250$ for the *full-RQMC* method not to affect the convergence law results. Results are presented in Fig. 4. Here again, *Standard-MC, SFS* and *FFS* methods exhibit a 1/2-convergence-rate law. *SFS and FFS methods* perform slightly better than the *Standard-MC* method when looking at the obtained relative standard deviation. In this configuration, the scattering

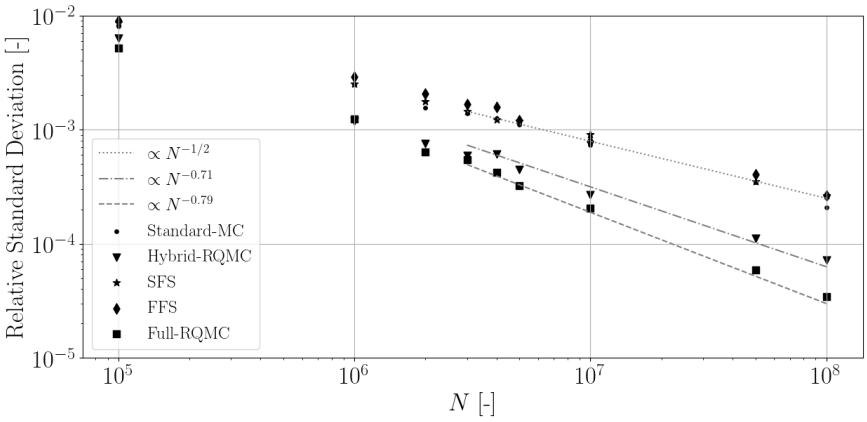

Figure 3: Relative standard deviation of computed wall emittance as a function of the total number of rays N for the five considered cases. Conditions: $\tau_L = 0.2$ and $\omega = 0.3$. Convergence rates are also displayed in dashed lines.

phenomenon is dominant but occurs often. Hence, forcing the ray to scatter has a little impact on the error than the *Standard-MC* method without forced-scattering. The *full-RQMC* convergence rate is barely affected compared to the case with an albedo equals to 0.3 and still outperforms all the methods. Finally, the *Hybrid-RQMC* convergence rate becomes closer to 1/2, which confirms that the MC scattering treatment limits the convergence rate of the hybrid method. The *full-RQMC* approach appears more interesting as its convergence properties are less sensitive to the weight of scattering.

A third case is finally considered to emphasize the effects of fast-forced-scattering by considering an optical thickness $\tau_L = 0.1$ and an albedo $\omega = 0.9$. In this configuration, the radiative wall flux strongly depends on scattering, while the scattering event probability is low. Hence, the forced-scattering technique is expected to lessen the relative standard deviation in such a case significantly. This is indeed observed in Fig. 5. Almost ten times more realizations are needed for the standard MC computation to achieve a 10^{-4} relative error, demonstrating the benefits of the fast forced-scattering (FFS) technique in such conditions. It can be observed that the standard forced-scattering technique

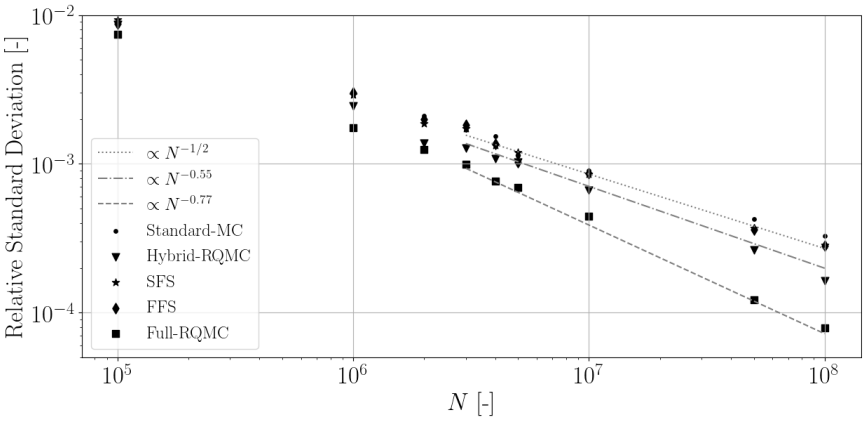

Figure 4: Relative standard deviation of computed wall emittance as a function of the total number of rays N for the five considered cases. Conditions: $\tau_L = 1$ and $\omega = 0.7$. Convergence rates are also displayed in dashed lines.

(SFS), gives similar results than the FFS, but with an increased CPU time due to the generation of τ^* as explained in Section 2.3.

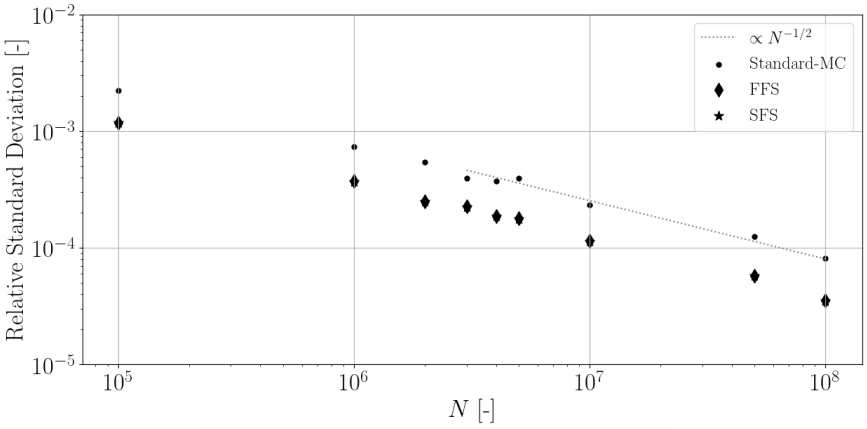

Figure 5: Relative standard deviation of computed wall emittance as a function of the total number of rays N for standard Monte Carlo case and Standard Forced Scattering and Fast-forced-scattering case. Conditions: $\tau_L = 0.1$ and $\omega = 0.9$. Convergence rate is also displayed in dashed lines.

3.3.3. Convergence performance : combination of methods

Previous sections have shown the efficiency of the *full-RQMC* approach. It is here combined with forced-scattering to assess the impact on the convergence rate. Results for three cases are compared: the previous *Standard-MC* and *full-RQMC* cases, and the full-RQMC computation combined with fast forced-scattering technique referred as *full-RQMC-FFS*.

Figure 6 compares the results for the three cases for the conditions $\tau_L = 1$ and $\omega = 0.7$. It can be observed that the *full-RQMC-FFS* case is the most accurate: applying the variance reduction technique to favor scattering events on the *full-RQMC* case shifts the relative standard deviation to lower values. Besides, the power-law coefficient of the convergence rate for *full-RQMC* and *full-RQMC-FFS* cases is similar. In other words, using variance reduction techniques along with the RQMC method preserves its benefits and lessen the number of realizations required.

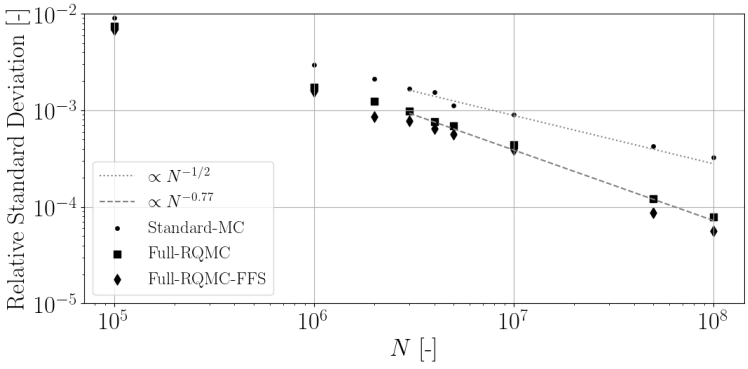

Figure 6: Comparison of relative standard deviation for the computed wall emittance as a function of the total number of rays N for the cases *full-RQMC* and *full-RQMC-FFS*. Conditions: $\tau_L = 1$ and $\omega = 0.7$. Convergence rate is also displayed in dashed lines.

The benefits from the fast-forced-scattering technique is quite low since scattering already occurs often in this condition ($\tau_L = 1$, $\omega = 0.7$). Hence, the three methods are also considered with $\tau_L = 0.1$, $\omega = 0.9$ in order to emphasize

FFS effects, and are presented Fig. 7. It is observed that the RQMC technique enables again to enhance the convergence rate. For the studied condition, combining RQMC with the FFS technique achieves a greater improvement than in the aforementioned conditions. The results in Fig. 7 are shifted downwards, and the convergence rate exponent is similar to the one obtained in the *Full-RQMC* case.

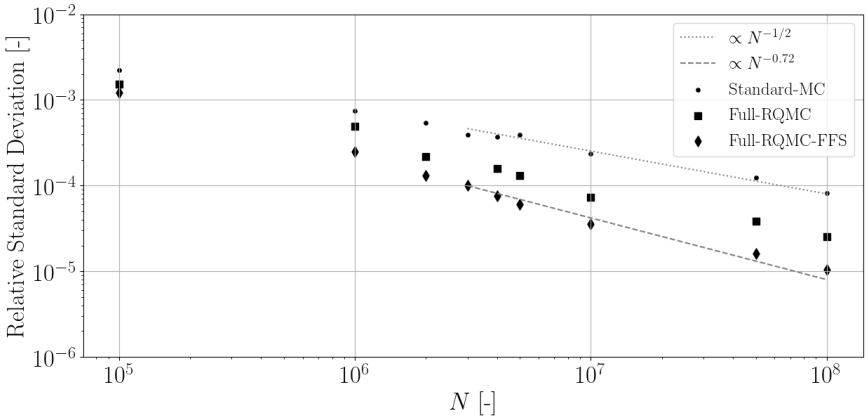

Figure 7: Comparison of relative standard deviation for the computed wall emittance as a function of the total number of rays N for the cases *full-RQMC* and *full-RQMC-FFS*. Conditions: $\tau_L = 0.1$ and $\omega = 0.9$. Convergence rate is also displayed in dashed lines.

3.4. Impact of the value of s_{max} on the performance of the full-RQMC method

In the previous section, the performance of the *full-RQMC* case has been assessed for different conditions with appropriate values of s_{max}. This part's objective is to *a-posteriori* justify the chosen values by studying the obtained convergence rate for several values of s_{max}. The Monte Carlo computational parameters are identical as those defined in Sec. 3.3.2, only s_{max} is allowed to vary. Only the *full-RQMC* case (without forced-scattering) is considered to isolate the impact of the Sobol sequence dimension.

Table 1 shows the evolution of the convergence rate obtained for the various considered cases.

Number of max. scattering	Convergence rate exponent		
s_{max}	$\tau_L = 0.2$, $\omega = 0.3$	$\tau_L = 1$, $\omega = 0.7$	$\tau_L = 0.1$, $\omega = 0.9$
1	0.504	0.502	0.501
3	0.53	0.503	0.505
10	0.58	0.53	0.51
20	0.61	0.58	0.53
30	0.7	0.6	0.59
50	**0.8**	0.68	0.64
100	0.804	0.768	0.71
250	0.805	**0.77**	**0.72**

Table 1: Evolution of the convergence rate exponent in function of the maximum number of scattering events s_{max} used to build the Sobol sequence for the RQMC method. The retained convergence rate in Sec. 3.2 are emphasized in bold fonts.

For a low Sobol dimension corresponding to a low s_{max} value, the convergence rate is identical to the expected Monte Carlo convergence rate. This is explained by the fact that, once the number s_{max} of scattering events is reached, the solver switches from the RQMC cubature rule to a standard Monte Carlo sampling. When s_{max} increases, the convergence rate is improved until it reaches a given value indicating the final numerical result's sensitivity to the number of scattering events. The plateau is reached for different values depending on the albedo and the optical thickness. Then, one should be aware of such property to maximize RQMC efficiency. *A priori* evaluation of s_{max} should be considered before carrying out any expansive RQMC simulations with scattering. The three previous values considered for s_{max} correspond to the convergence rate law's converged values. The previously reported RQMC convergence rates are not notably affected by choice of a higher number of scattering events.

4. Modelling of thermal radiation in sooted flames

This section introduces the radiative models used to calculate the radiative power in the turbulent sooting jet flame presented in Section 5.

4.1. Gaseous radiative properties

Only the radiative properties of CO_2 and H_2O are considered. The cK model, based on updated parameters from Riviere and Soufiani [15], is used to describe the gas radiative properties. For H_2O, 44 spectral bands are considered up to 9200 cm^{-1}. CO_2 absorbs radiation in 17 of these bands. For each gaseous component, a 7-point Gauss quadrature is used per band. In the 17 overlapping bands, 49 quadrature points are used. The cK database is then made of 1022 pseudo-spectral points.

4.2. Soot radiative properties

A total of 93 spectral bands up to 29 000 cm^{-1} are added into the cK-model. Soot radiative properties depend on their optical properties and their morphology. In this study, the interaction phenomenon between primary particles of an aggregate such as overlapping or necking [23] is neglected.

4.2.1. Soot optical properties

The complex index of refraction of soot particles, noted $m = n - ik$, characterizes soot optical properties. The real part n is the refractive index, and the imaginary part k is the absorptive index. In the literature, two models are mostly encountered for n and k : a constant formulation as proposed in [44] and a wavelength λ dependency. The second model is here retained, given by [45]:

$$\begin{aligned} n(\lambda) &= 1.811 + 0.1263\,\ln\lambda + 0.027\,\ln^2\lambda + 0.0417\,\ln^3\lambda \\ k(\lambda) &= 0.5821 + 0.1213\,\ln\lambda + 0.2309\,\ln^2\lambda + 0.01\,\ln^3\lambda \end{aligned} \tag{14}$$

The expression is provided for λ from 0.2 to 6 μm.

4.2.2. Soot morphology

The retained model for soot morphology considers soot particles as spherical below a given volume V_{LIM} and as aggregates otherwise. These aggregates are characterized by a number of primary spherical particles n_P of diameter d_P. These two quantities are given by the following relations :

$$\begin{aligned} n_P &= \frac{S^3}{36\pi V^2} \\ d_P &= \frac{6V}{S} \end{aligned} \tag{15}$$

where S is the aggregate surface, and V its volume. To close these relations, a relation between the surface and the volume of an aggregate is required. The same law as in [46] is retained: the model has been derived by fitting numerical results obtained on 1D laminar premixed ethylene flames [47, 48], leading to

$$S = \begin{cases} \left(V/V_{C_2}\right)^{2/3} S_{C_2} \text{ for } V < V_{LIM} \\ \left(V/V_{C_2}\right)^{\theta(V)/3} S_{C_2} \text{ for } V > V_{LIM} \end{cases} \tag{16}$$

with $S_{C_2} = 0.372$ nm^2 and $V_{C_2} = 0.021$ nm^3 the surface and the volume of a spherical molecule composed by two atoms of carbon. The limit volume V_{LIM} is equal to $10^{2.6}$ nm^3. $\theta(V)$ is given by :

$$\theta(V) = 3.0 \cdot \frac{\left(\log\left(V/V_{LIM}\right)\right) + 2/3 \cdot \left(\log\left(V_{LIM}/V_{C_2}\right)\right)}{\log\left(V/V_{C_2}\right)} \tag{17}$$

4.2.3. Rayleigh-Debye-Gans theory for Fractal Aggregates

The Rayleigh-Debye-Gans theory (RDG-FA) derived in [22, 49] extends the Rayleigh theory for spherical particles by assuming an aggregate shape for soot. An aggregate is composed of an ensemble of monodisperse spherical primary particles. The model assumes that the soot optical refraction index $m = n - ik$ is close to unity and that the size parameter $x_P = \frac{\pi d_P}{\lambda}$ is smaller than unity. For the considered wavelengths, the maximum size parameter varies from 0.03 to 0.15. The modulus of m, $|m|$ varies from 0.85 to 1.58. The model's assumptions appear here questionable, especially for small wevalength. However, RDG-FA in fact yields a good description of scattering properties for aggregates

in wider conditions that the initial assumptions [6, 50]. In the original RDG-FA model, overlapping and necking phenomena between the primary particles of the aggregate are neglected. A recent work has extended the RDG-FA theory for such cases [23]. Corrective parameters have been obtained by fitting results obtained with an accurate model: the Discrete Dipole Approximation. However, no analytical expression has been provided so far. Moreover, given that overlapping and necking information is still out of reach in CFD simulations of sooted flames, the corresponding effects are not considered in the following. The polydispersity of primary particles diameter have also been considered in this theory [51] with new corrective parameters. In the corresponding study, the effect of polydispersity is found to be of a second order effect compared to the internal multiple scattering, which is also out of reach in CFD simulations. Therefore, the polydispersity of primary particles has also been neglected.

Soot absorption coefficient.

The soot absorption coefficient is given by :

$$\kappa_\lambda^{soot} = \int_0^{+\infty} C_{abs,agg}(V) n(V)\,\mathrm{d}V = \frac{6\pi E(m) f_V}{\lambda} \tag{18}$$

where $C_{abs,agg}$ is the absorption cross-section coefficient of the aggregate, V the soot particle volume, λ the wavelength, $n(V)$, the particle number density. An analytical expression is obtained, equivalent to the one obtained from Rayleigh's theory, where f_V is the soot volume fraction and $E(m)$ is given by the complex index of refraction :

$$E(m) = -\mathcal{I}m\left\{\frac{m^2-1}{m^2+2}\right\} = \frac{6nk}{(n^2-k^2+2)^2+4n^2k^2} \tag{19}$$

Soot scattering coefficient.

The soot scattering coefficient is defined by the following expression:

$$\sigma_\lambda^{soot} = \int_0^{+\infty} C_{scat,agg}(V) n(V)\,\mathrm{d}V \tag{20}$$

According to the RDG-FA theory, the scattering cross-section coefficient of an aggregate $C_{scat,agg}$ is written :

$$C_{scat,agg} = n_P^2 \, C_{scat,part} \, g(k, R_g) \tag{21}$$

where n_P is the number of primary particles which forms the aggregate, $C_{scat,part}$ is the scattering cross-section coefficient of a primary particle based on Rayleigh theory. g is a factor introduced in [22] that depends on R_g, the gyration radius of the aggregate, and $k' = 2\pi/\lambda$. $C_{scat,part}$ and g are calculated as follows:

$$\begin{aligned} C_{scat,part} &= \frac{8}{3k'^2}\pi x_P^6 F(m) \quad \text{with} \quad F(m) = \left|\frac{m^2-1}{m^2+2}\right|^2 \\ g(k', R_g) &= \left(1 + \frac{4k'^2 R_g^2}{3D_f}\right)^{-D_{f/2}} \end{aligned} \tag{22}$$

Experimentally, it has been observed that soot particles forms look-alike fractal aggregates. These aggregates are described by the following empirical law [9]:

$$n_P = k_f \left(\frac{2R_g}{d_P}\right)^{D_f} \tag{23}$$

D_f and k_f are the fractal parameters, fixed in the simulations, respectively to 1.8 and 1.3, such as in the RDG-FA theory [22]. Hence, Equation 23 provides an expression for R_g, which enables to compute $C_{scat,agg}$ given in Equation 21. However, there is no simple analytical expression for σ_λ^{soot}. Hence, numerical integration of equation 20 is required.

Soot phase function.

The phase function for an ensemble of aggregates can be defined by an integral formulation involving the number density function $n(V)$:

$$\Phi_{glob}(\theta) = \int_V \Phi_{agg}(\theta) n(V) dV \tag{24}$$

The scattering-phase function of a particular aggregate is defined by

$$\Phi_{agg}(\theta) = \frac{4\pi}{C_{sca,agg}} \frac{C_{vv,agg}(\theta) + C_{hh,agg}(\theta)}{2} \tag{25}$$

where θ is the angle of scattering, $C_{vv,agg}$ and $C_{dd,agg}$ are the differential scattering cross-sections. In the RDG-FA theory, these two cross-sections are given by :

$$\begin{aligned} C_{vv,agg}(\theta) &= n_P^2\, C_{vv,part}\, f\left(qR_g\right) \\ C_{hh,agg}(\theta) &= n_P^2\, C_{hh,part}\, f\left(qR_g\right) \\ C_{vv,part} &= \frac{C_{hh,part}}{\cos(\theta)^2} = \frac{x_p^6 F(m)}{k'^2} \end{aligned} \tag{26}$$

The quantity f, is the structure factor and is discussed in the review of Sorensen [52]. In this work, a recent formulation [12] is retained and given by :

$$f\left(qR_g\right) = \left(1 + \frac{8\left(qR_g\right)^2}{3D_f} + \left(qR_g\right)^8\right)^{-D_f/8} \tag{27}$$

where $q = \frac{4\pi \sin(\frac{\theta}{2})}{\lambda}$ is the modulus of the scattering vector.

By combining equations 21 and 26 and inserting into Eq. 25, one obtains the general expression of the phase function for one aggregate :

$$\Phi_{agg}(\theta) = \frac{3f\left(qR_g\right)\ \left(1+\cos^2(\theta)\right)}{4\ g(k', R_g)} \tag{28}$$

In the Rayleigh regime (small particles), we have $f = g = 1$, and Eq. 28 reduces to $\Phi_{Rayleigh}(\theta) = \frac{3(1+\cos^2(\theta))}{4}$. Figure 8 compares the phase functions obtained with the RDG-FA model, using Eq. 28, and $\Phi_{Rayleigh}$. The considered aggregate is composed of $n_P = 256$ primary particles, with three different diameters d_P: 1 nm (left), 10 nm (center), 50 nm (right), at a fixed wavelength of 534nm. As expected, the discrepancy between the two models increases with the size of the primary particle diameter. The polar representation exhibits the scattering phase function's behavior, *i.e.* the probability to be scattered in a given direction. It is clear that, for the Rayleigh regime, the scattering phase function is symmetric. However, for the RDG-FA theory, forward scattering is

strongly favored (as the polar plot is shifted to the right) for the biggest primary particle. This behavior has also been observed experimentally [53], and with aggregates generated numerically [6] .

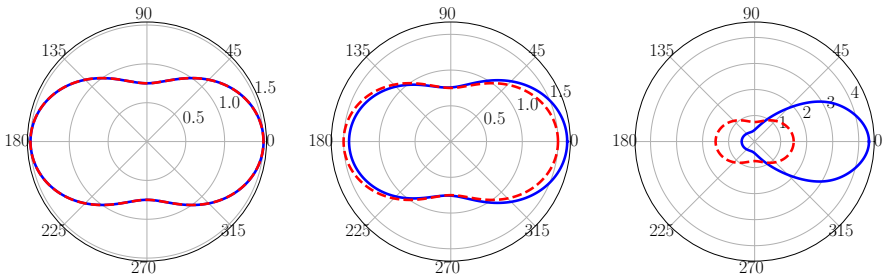

Figure 8: Comparison of phase functions between Rayleigh theory (red dashed lines) and RDG-FA theory (blue line) for a given aggregate with 3 different primary particle diameters d_p = 1 nm (left), 10 nm (center) and 50 nm (right).

It is important to note that, the overall effect of scattering is not only linked to the phase function but also to the scattering coefficient σ. Because the expressions between Rayleigh and RDGFA differ for the scattering cross-section, the resulting scattering coefficient is different. For the three patterns presented Fig.8, the albedo $\omega = \frac{\sigma}{\kappa+\sigma}$ is respectively :

- Left ($d_p = 1$ nm) : $\omega_{rayleigh} = 3 \times 10^{-4}$ and $\omega_{RDGFA} = 0.1$
- Center $d_p = 10$ nm) : $\omega_{rayleigh} = 4 \times 10^{-2}$ and $\omega_{RDGFA} = 0.6$
- Right ($d_p = 50$ nm) : $\omega_{rayleigh} = 0.8$ and $\omega_{RDGFA} = 0.95$

It can be observed that, although the scattering phase functions are similar for on the left and center in Figure 8, the albedo strongly differs due to the difference in scattering cross-section expressions. Therefore, the impact of scattering can be important for particles with an intermediate size in primary particles.

4.3. Validation of RDG-FA methodology

The implementation of the RDG-FA theory in RAINIER is validated against published numerical results of radiative heat transfer obtained with a Discrete Ordinates Method calculation [54].

The computational domain is a 3D cubic box with a length of $L = 1$ m, with 100x100x10 points in the direction x, y and z, respectively. The black walls temperature are set to $T_w = 300$ K while the domain is set to $T_{dom} = 2000$ K. The domain is composed of homogeneous soot aggregates with $n_p = 256$ primary particles and $d_p = 50$ nm. The soot volume fraction is set to $f_V = 10^{-6}$. Small changes from the previously described setup are considered to be consistent with the model for soot radiative properties retained in [54]. The optical index of soot particles m is chosen with a spectral dependency whose parameters are taken from [55]. The form factor expression f is taken from the original RDG-FA model, which differs from Equation 27. This set-up is refered to **"Original set-up"** in the following.

The Monte Carlo simulations are carried out using the *full-RQMC-FFS* method that combines RQMC and fast-forced-scattering. s_{max} is fixed at 200, and the maximum length for the fast-forced-scattering method is set to $L_{max} = 1$ m. The controlled error is set to 0.5% for relative standard deviation. Such a fine accuracy is required to capture scattering effects correctly. The obtained radiative power profile is displayed in Figure 9.

Results are in excellent agreement with the discrete ordinate methods calculation. However, it appears that the effects of scattering are small in this configuration. To achieve a thorough validation of the scattering formulation, the predicted spectral radiative power difference with and without scattering is compared. The relative difference $\frac{P_{scattering} - P_{no-scattering}}{P_{no-scattering}}$ is computed and averaged for several points on the mid-plane of the domain. It is shown in Fig. 10 as a function of the spectral wavelength. The figure illustrates the known effect of soot scattering, which increases drastically for small wavelengths. Both numerical results are very close. The error bars (0.5%) associated with the simulation with scattering are also shown around the predicted curve. For high

wavelength, scattering effects diminish, which requires an accurate control to be captured. Negligible differences between the predicted profile and results in [54] are attributed to remaining statistical noise in the present results outlined by the error bars, and numerical errors in the Discrete Ordinates Method calculation of the original study.

It this important to recall that the form-factor and optical index m expressions considered in the following are not the same as the ones used in the validation case. In Figure 10, results are also computed with the updated set-up (which is referred to **Retained set-up**). The difference in optical soot properties and form-factor quantitatively affects the spectral profile throughout the whole range of wavelengths.

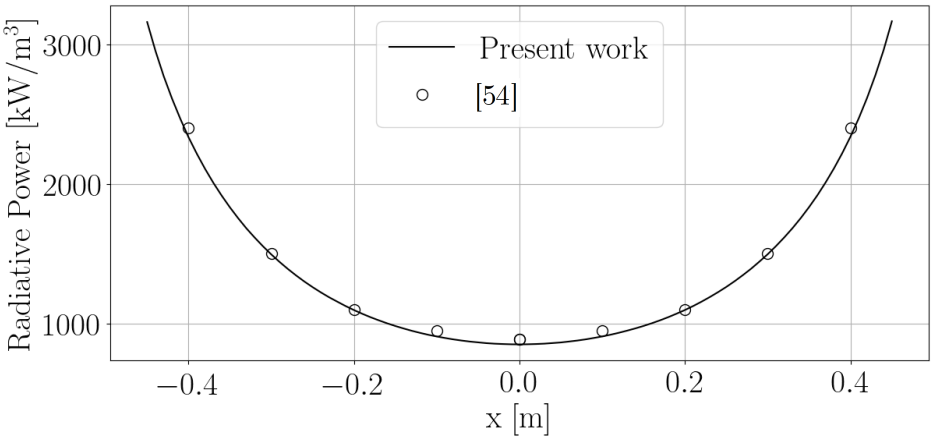

Figure 9: Profile of radiative power along the domain composed of soot aggregates and comparison with Ref. [54].

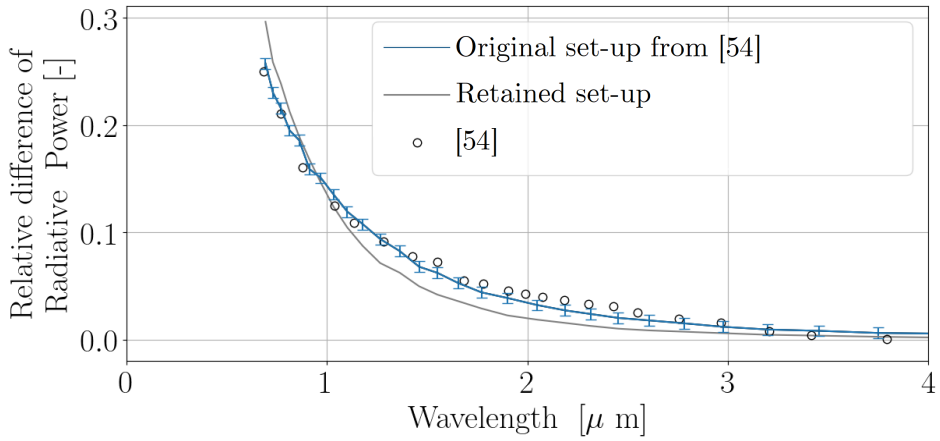

Figure 10: Relative difference in spectral radiative power with and without scattering for both RDG-FA setups.

5. Computation of radiative heat transfer in a turbulent sooted jet flame

In this section, all Monte Carlo calculations are performed using the RDG-FA model presented in Sec. 4.2.3.

5.1. Reference fields

The studied configuration is the turbulent jet diffusion flame experimentally studied at Sandia [35]. It is a diffusion, non-confined turbulent jet flame under standard atmospheric conditions. The fuel pipe is fed with pure ethylene. This configuration corresponds to a turbulent jet with Reynolds number Re_D = 20 000, based on the fuel jet diameter D = 3.2mm. The corresponding bulk velocity is v_{fuel} = 54.7 m/s. The main jet tube presents an outer diameter of 4.6 mm and is surrounded by a coflow (inner diameter: 15.2 mm; outer diameter: 19.1 mm). The mesh contains 10 million cells and 1.7M nodes. The typical cell size at the jet exit is $\Delta x \approx 0.20$mm and increases up to 5 mm further downstream.

The reference fields considered for the present study are taken from previous works on this flame [21] based on coupled large-eddy simulation (LES) to study soot formation and radiation. In Rodrigues and co-workers' work, the soot formation modeling relies on a sectional method [46], which gives here access to the soot number density function $n(V)$. LES fields are provided to the Monte Carlo solver to compute radiative fields while accounting for scattering, which was neglected in the previous numerical study. The objective is here to quantify this assumption accurately. Figure 11 presents the temperature, soot volume fraction fields used in this study, and the corresponding radiative power field computed by the Rainier solver.

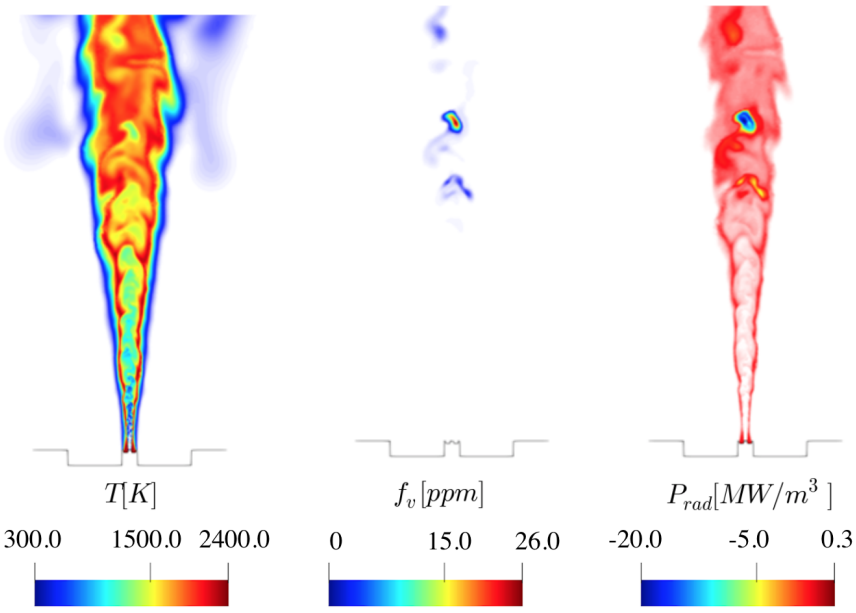

Figure 11: Left: reference fields of temperature and soot volume fraction. Right: computed radiative power field.

In most parts of the domain, the radiative power is governed by hot participating gases. Soot particles are present where the mixture is rich, and the

temperature is high before oxidized. In this zone, the high instantaneous soot volume fraction (25 ppm) strongly impacts the radiative power.

The following solution data are given to the Rainier solver: pressure, molar fractions of CO_2 and H_2O, soot volume fraction f_v, and the soot number density function $n(V)$ discretized in 25 sections. For all Monte Carlo computations, the inlet and the outlet of the domain are considered as non-reflective walls. The same mesh and geometry as in [21] are employed.

5.2. Quasi-Monte Carlo performance tests

Convergence properties of the RQMC method derived to take into account scattering are first presented. Two different tests are carried out on the turbulent jet flame configuration. The first test consists of imposing the same total number of rays N, introduced in Section 2.4.3 with the same number of trials $M = 100$, at all the points where the radiative power is computed. The achieved error measured by the relative standard deviation of the result is checked at every node. In the second test, convergence criteria are imposed on the desired standard deviation: 0.1% for the relative value and 0.1% of the maximum radiative power for the absolute value. In this case, the number of rays is not fixed and will vary in the domain. Two computations are compared: the *Standard-MC* and *full-RQMC-FFS* cases. The latter case should achieve fast convergence by combining fast forced-scattering and RQMC cubature applied to emission, absorption, and scattering ($s_{max} = 300$).

5.2.1. Test 1: fixed number of rays

This test indicates which zones are easily converged or not. The accuracy for the prescribed number of rays in both computations is characterized by the radiative power's local relative standard deviation. Results for *Standard-MC* and *full-RQMC-FFS* cases are compared in Fig. 12. Different convergence properties at each node yield an inhomogeneous error field. The relative standard deviation is the highest in low-temperature regions where the radiative power is small, which is not critical. This is also a known shortcoming of the

considered ERM Monte Carlo method that convergences weakly in cold regions dominated by absorption. It can be seen nonetheless that the computation based on RQMC gives a smaller error field throughout the domain, indicating a faster convergence for this case.

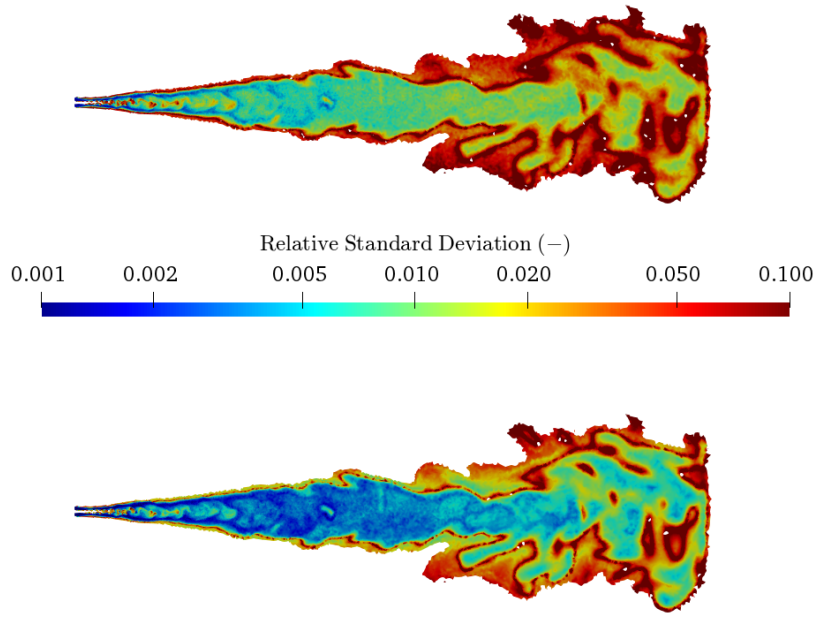

Figure 12: Comparison of relative standard deviation fields in the turbulent jet flame. **Top**: *Standard-MC*. **Bottom**: *full-RQMC-FFS*.

The convergence rate is studied further by considering the evolution of the number of rays' standard deviation at a given point. Since we are focusing on the scattering by soot particles, we choose the location where the soot volume fraction is maximum ($x = 0.4$ m). The convergence plot similar to the ones presented in Sec. 3 is shown in Fig. 13. As expected, the asymptotic convergence law is proportional to $N^{-1/2}$ for the *Standard-MC* case while Quasi-Monte Carlo achieves a faster convergence rate whose exponent coefficient is close to 0.73. Hence, reaching a relative error of 10^{-3} requires approximatively 10 times more

rays for the standard MC approach.

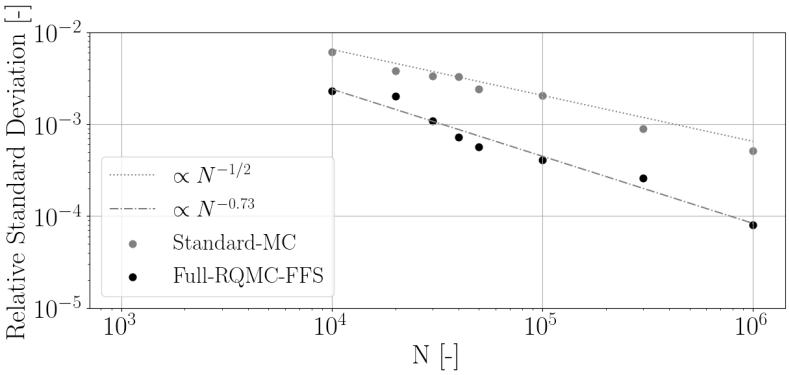

Figure 13: Relative standard deviation as a function of the number of rays N at the location of maximum soot volume fraction.

5.2.2. Test 2: controlled error

In Figure 12, an inhomogeneous convergence is observed. Some zones can be considered too accurate, while others suffer from poor convergence. Performing a simulation with a controlled error enables more efficient computation of the radiative power. The fields of the number of rays required to achieve the accuracy criteria in Test 2 are displayed in Fig. 14. Thanks to the absolute error criterion, ill-converged regions of the negligible contribution surrounding the flame are disregarded. In both cases, the regions where soot particles are present, and the temperature is low is where the required number of rays is the highest. Clearly, with the QMC methodology combined with forced scattering, the number of rays required to achieve the prescribed error is much lower than with the *Standard-MC* case. In terms of CPU time, the *Standard-MC* case requires 850 seconds on 96 CPUs to achieve the prescribed error while the *full-RQMC-FSS* case takes 415 seconds. A twofold speed-up factor is then obtained, which is a significant improvement in computational time.

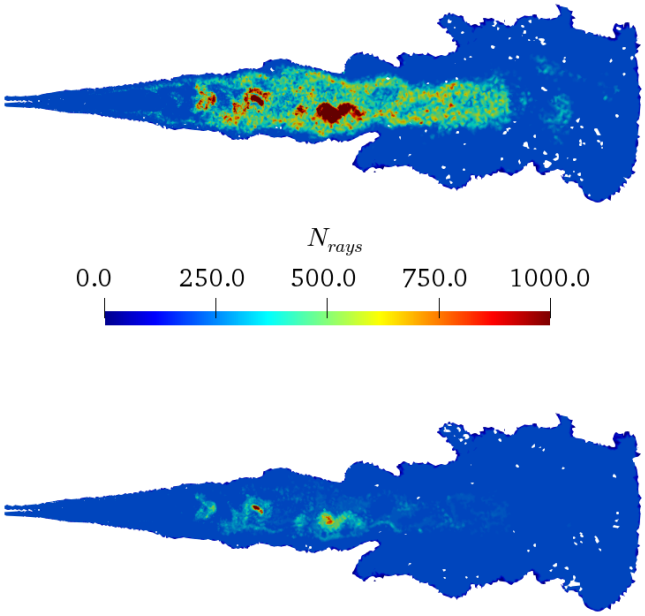

Figure 14: Comparison of the number of rays required to reach a given error on the Sandia's turbulent jet flame. **Top** : *Standard-MC*, **Bottom** : *full-RQMC-full*.

5.3. Impact of scattering

As previously mentioned, scattering was neglected in the coupled calculations performed on this turbulent jet flame [21]. Such an assumption is based on the scattering coefficient's expression using the Rayleigh theory: the absorption coefficient is proportional to x, the size parameter, while the scattering parameter is proportional to x^4. Since $x \approx 0.1$ here, one expects that absorption totally dominates scattering. However, when considering the RDG-FA theory, the scattering coefficient is related to the square of the number of primary particles n_p^2 that can be large (n_p is around several hundred). Therefore, accurate computation of scattering effects with the developed RQMC method and state-of-the-art soot radiative properties is required to assess *a posteriori* the hypothesis previously used in the coupled computation. The previously as-

sessed *full-RQMC-FSS* method is used to achieve high accuracy at an affordable cost.

The scattering impact in the jet flame configuration is assessed with two computations: one accounting for scattering and another without. Since the scattering effect is expected to be low nonetheless, the calculations need to be extremely accurate. The prescribed accuracy is based on local relative and absolute standard deviations that are then equal to 0.1% and 0.1 % of the maximum radiative power.

The radiative power along the centerline for the two cases is presented in Fig. 15. Only the zone with the soot volume fraction peak is displayed. Both computations with and without scattering give similar results. For both profiles, a decrease in radiative power magnitude is observed at the soot volume fraction peak. This is due to the corresponding lower temperature at this position coming from the considered fields issued from coupled simulations: the local temperature is reduced due to soot radiation, which, in turn, diminishes the magnitude of heat losses. Both cases differ only slightly, confirming a small effect of soot scattering in the studied flame. This has however been properly assessed with the RDG-FA model.

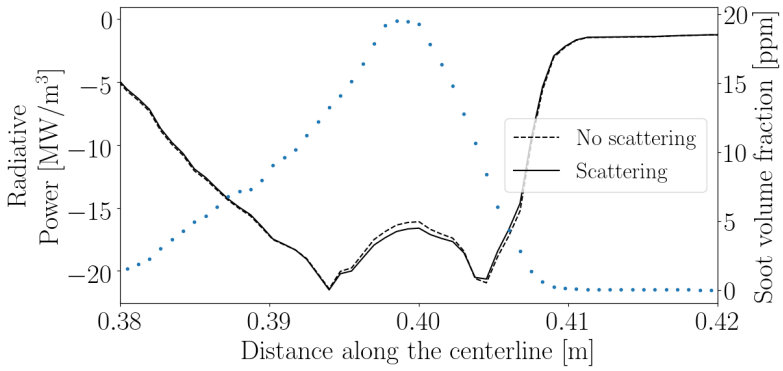

Figure 15: Comparison of radiative power profiles (left axis, solid and dashed lines) along the jet flame centerline. The plotted region corresponds to the peak in soot volume fraction (right-axis, dotted line).

Monte Carlo simulations need to be very accurate to capture such effects in the present flame. The difference between both radiative power profiles in Fig. 15 is plotted Fig. 16. The error bounds, which here fulfill the accuracy condition based on 0.1 % of the maximum radiative power, outline that the results can be interpreted confidently. The statistical noise is lower than the observed difference. The same computation has been carried out with the standard Rayleigh model. The corresponding difference between the case with and without scattering is also shown in Fig. 16. The scattering contribution with the Rayleigh model is so small that it is not distinguished in the statistical noise. Indeed, the Rayleigh model applied to soot aggregates strongly underestimates scattering compared to RDG-FA theory. Hence, relying on Rayleigh's theory to a priori exclude soot scattering is not safe. The present study has allowed quantifying such effects in the investigated flame that amounts here to a few percent of the local radiative power.

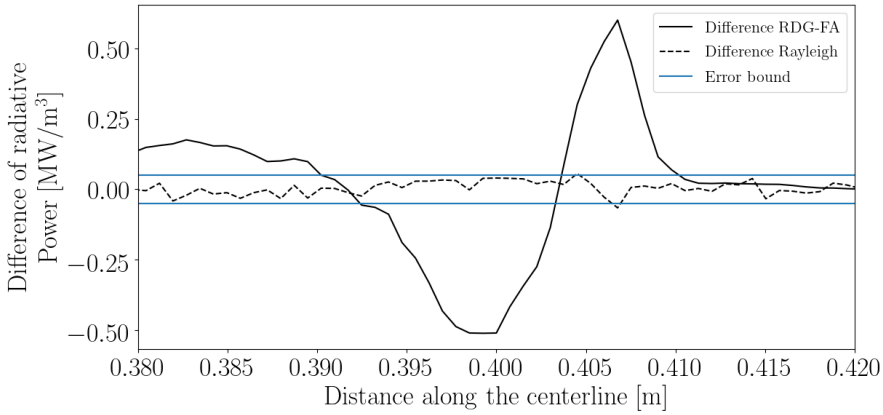

Figure 16: Difference of radiative power along the centerline with and without scattering for RDG-FA (solid line) and Rayleigh (dashed line) theories. Error bounds corresponding to the results' standard deviation are shown in plain horizontal lines.

6. Conclusions

The increase in computational resources and numerical algorithms' advances enables accurate Monte Carlo methods to solve radiative heat transfer in 3D configurations. Such methods can even be used nowadays in coupled simulation workflows where thermal radiation, turbulence, and combustion are solved simultaneously. These computations remain expansive and benefit strongly from any improvements on the Monte Carlo solver. In particular, the Quasi-Monte Carlo cubature provides a very interesting methodology to accelerate the convergence of Monte Carlo estimates.

In this study, the treatment of scattering with a randomized Quasi-Monte Carlo (RQMC) method has been investigated. Different variants have been derived and assessed in homogeneous slabs with various conditions of optical thickness and albedo. In all the presented cases, a significant improvement in the convergence rate has been demonstrated: the same accuracy can be achieved with much less realizations, which shows the benefits and the superiority of RQMC method compared to the standard MC.

It was shown that the accuracy is even more increased by considering a maximum number of scattering events in the RQMC sampling and by combining the approach with forced-scattering. The latter property outlines that the RQMC method is independent of any variance reduction techniques: it can benefit from the large set of Monte Carlo acceleration techniques to be further improved.

The method has been applied to a sooted turbulent jet flame. Large-eddy simulation fields from a coupled computation, where soot scattering was neglected, are considered. Such a hypothesis has always been retained so far in CFD studies accounting for soot radiation. However, the proposed justification relies on Rayleigh's theory, which is not valid for soot aggregates. An up-to-date description of soot scattering properties with RDG-FA theory has then been considered to quantify correctly such effects in the studied flame. The derived RQMC method estimates this contribution accurately and efficiently since it appears small. Such observation a-posteriori justifies the choice to neglect the

scattering in previous calculations of this configurations [20, 21]. The convergence rate analysis in this turbulent flame configuration also confirms the new Monte Carlo method's significant improvement. Indeed, at the soot volume fraction peak location, the same error can be achieved locally with approximatively 10 times fewer rays than the standard MC method.

While soot scattering effects are small in this case, let us outline that RDG-FA theory is highly sensitive to the soot morphology and particle size distribution. Larger effects could then be encountered in other operating conditions. Finally, several optical diagnostics to characterize soot morphology are based on soot scattering properties. Simulating these diagnostics and then scattering from soot particles is of great interest to understand the signals observed experimentally.

7. Acknowledgement

The authors gratefully acknowledge the financial support within the EU Horizon 2020 Soot Processes and Radiation in Aeronautical Innovative Combustion (SOPRANO) project (Grant Agreement No. 690724). Furthermore, the work was performed using HPC resources from GENCI-CINES (Grant 2019-A0062B10159) as well as from the "Mésocentre" computing center of CentraleSupélec and École Normale Supérieure Paris-Saclay supported by CNRS and Région Île-de-France (http://mesocentre.centralesupelec.fr/)

8. References

References

[1] A. H. Lefebvre, Flame radiation in gas turbine combustion chambers, International Journal of Heat and Mass Transfer 27 (1984) 1493–1510.

[2] H. I. Joo, Ö. L. Gülder, Experimental study of soot and temperature field structure of laminar co-flow ethylene-air diffusion flames with nitrogen dilution at elevated pressures, Combustion and Flame 158 (2011) 416–422.

[3] H. M. Amin, A. Bennett, W. L. Roberts, Determining fractal properties of soot aggregates and primary particle size distribution in counterflow flames up to 10 atm, Proceedings of the Combustion Institute (2019) 1161–1168.

[4] S. A. Steinmetz, T. Fang, W. L. Roberts, Soot particle size measurements in ethylene diffusion flames at elevated pressures, Combustion and Flame 169 (2016) 85–93.

[5] B. Gigone, A. E. Karata, Ö. L. Gülder, Soot aggregate morphology in coflow laminar ethylene diffusion flames at elevated pressures, Proceedings of the Combustion Institute 37 (2019) 841–848.

[6] F. Liu, C. Wong, D. R. Snelling, G. J. Smallwood, Investigation of absorption and scattering properties of soot aggregates of different fractal dimension at 532 nm Using RDG and GMM, Aerosol Science and Technology 47 (2013) 1393–1405.

[7] Ü. Ö. Köylü, G. M. Faeth, Radiative Properties of Flame-Generated Soot, International Geophysics 115 (1993) 409–417.

[8] Ü. Ö. Köylü, G. M. Faeth, T. L. Farias, M. G. Carvalho, Fractal and projected structure properties of soot aggregates, Combustion and Flame 100 (1995) 621–633.

[9] R. J. Samson, G. W. Mulholland, J. W. Gentry, Structural Analysis of Soot Agglomerates, Langmuir 3 (1987) 272–281.

[10] T. Ni, J. A. Pinson, S. Gupta, R. J. Santoro, Two-dimensional imaging of soot volume fraction by the use of laser-induced incandescence, Applied Optics 34 (1995) 7083–7091.

[11] H. Geitlinger, T. Streibel, R. Suntz, H. Bockhorn, Two-dimensional imaging of soot volume fractions, particle number densities, and particle radii in laminar and turbulent diffusion flames, Symposium (International) on Combustion 27 (1998) 1613–1621.

[12] B. Yang, B. Hu, U. O. Koylu, Mean soot volume fractions in turbulent hydrocarbon flames: A comparison of sampling and laser measurements, Combustion Science and Technology 177 (2005) 1603–1626.

[13] H. M. Amin, W. L. Roberts, Soot measurements by two angle scattering and extinction in an N2-diluted ethylene/air counterflow diffusion flame from 2 to 5 atm, Proceedings of the Combustion Institute 36 (2017) 861–869.

[14] M. F. Modest, Radiative heat transfer, 2003.

[15] P. Rivière, A. Soufiani, Updated band model parameters for H_2O, CO_2, CH_4 and CO radiation at high temperature, International Journal of Heat and Mass Transfer 55 (2012) 3349–3358.

[16] T. Ren, M. F. Modest, D. C. Haworth, Simulating turbulence–radiation interactions using a presumed probability density function method, International Journal of Heat and Mass Transfer 121 (2018) 911–923.

[17] L. Tessé, F. Dupoirieux, J. Taine, Monte Carlo modeling of radiative transfer in a turbulent sooty flame, International Journal of Heat and Mass Transfer 47 (2004) 555–572.

[18] A. Gupta, D. C. Haworth, M. F. Modest, Turbulence-radiation interactions in large-eddy simulations of luminous and nonluminous nonpremixed flames, Proceedings of the Combustion Institute 34 (2013) 1281–1288.

[19] C. Koren, R. Vicquelin, O. Gicquel, Multiphysics Simulation Combining Large-Eddy Simulation, Wall Heat Conduction and Radiative Energy Transfer to Predict Wall Temperature Induced by a Confined Premixed Swirling Flame, Flow, Turbulence and Combustion 101 (2018) 77–102.

[20] R. S. Mehta, D. C. Haworth, M. F. Modest, Composition PDF/photon Monte Carlo modeling of moderately sooting turbulent jet flames, Combustion and Flame 157 (2010) 982–994.

[21] P. Rodrigues, O. Gicquel, B. Franzelli, N. Darabiha, R. Vicquelin, Analysis of radiative transfer in a turbulent sooting jet flame using a Monte Carlo method coupled to large eddy simulation, Journal of Quantitative Spectroscopy and Radiative Transfer 235 (2019) 187–203.

[22] R. Dobbins, C. M. Megaridis, Absorption and scattering of light by polydisperse aggregates., Applied optics 30 (1991) 4747–4754.

[23] J. Yon, A. Bescond, F. Liu, On the radiative properties of soot aggregates part 1: Necking and overlapping, Journal of Quantitative Spectroscopy and Radiative Transfer 162 (2015) 197–206.

[24] C. Peest, C. Schinke, R. Brendel, J. Schmidt, K. Bothe, Instrumentation-related uncertainty of reflectance and transmittance measurements with a two-channel spectrophotometer, Review of Scientific Instruments (2017).

[25] E. D. Cashwell, C. J. Everett, A Practical Manual on the Monte Carlo Method for Random Walk Problems, Mathematics of Computation (1960).

[26] M. Min, C. P. Dullemond, C. Dominik, A. De Koter, J. W. Hovenier, Radiative transfer in very optically thick circumstellar disks, Astronomy and Astrophysics 497 (2009) 155–166.

[27] I. Fredriksson, M. Larsson, T. Strömberg, Forced detection Monte Carlo algorithms for accelerated blood vessel image simulations, Journal of Biophotonics 2 (2009) 178–184.

[28] A. Feldick, A. Bansal, M. Modest, Variance Reduction Techniques For Monte Carlo Solution of Radiative Transfer in Hypersonic Flows Hybrid P1 Monte Carlo, 49th AIAA Aerospace Sciences (2011).

[29] M. Juvela, Efficient Monte Carlo methods for continuum radiative transfer, Astronomy and Astrophysics 440 (2005) 531–546.

[30] R. Buras, B. Mayer, Efficient unbiased variance reduction techniques for Monte Carlo simulations of radiative transfer in cloudy atmospheres: The

solution, Journal of Quantitative Spectroscopy and Radiative Transfer 112 (2011) 434 – 447.

[31] A. De Lataillade, J. L. Dufresne, M. El Hafi, V. Eymet, R. Fournier, A net-exchange Monte Carlo approach to radiation in optically thick systems, Journal of Quantitative Spectroscopy and Radiative Transfer 74 (2002) 563 – 584.

[32] L. Palluotto, N. Dumont, P. Rodrigues, O. Gicquel, R. Vicquelin, Assessment of randomized quasi-monte carlo method efficiency in radiative heat transfer simulations, Journal of Quantitative Spectroscopy and Radiative Transfer 236 (2019).

[33] J. Farmer, S. Roy, A quasi monte carlo solver for thermal radiation in participating media, Journal of Quantitative Spectroscopy and Radiative Transfer 242 (2020).

[34] J. M. Armengol, R. Vicquelin, A. Coussement, R. G. Santos, O. Gicquel, Scaling of heated plane jets with moderate radiative heat transfer in coupled DNS, International Journal of Heat and Mass Transfer 139 (2019) 456–474.

[35] ISF3, International sooting flame (ISF) workshop website, 2017.

[36] L. Tessé, F. Dupoirieux, B. Zamuner, J. Taine, Radiative transfer in real gases using reciprocal and forward Monte Carlo methods and a correlated-k approach, International Journal of Heat and Mass Transfer 45 (2002) 2797–2814.

[37] J. T. Farmer, J. R. Howell, Comparison of Monte Carlo Strategies for Radiative Transfer in Participating Media, Advances in Heat Transfer (1998).

[38] L. Tessé, Modélisation des transferts radiatifs dans les flammes turbulentes par une méthode de Monte Carlo, Ph.D. thesis, 2001.

[39] I. M. Sobol, Uniformly distributed sequences with an additional uniform property, USSR Computational Mathematics and Mathematical Physics 16 (1976) 236 – 242.

[40] P. L'Ecuyer, C. Lemieux, Recent advances in randomized quasi-monte carlo methods, 2016.

[41] S. Tezuka, H. Faure, I-binomial scrambling of digital nets and sequences, Journal of complexity 19 (2003) 744–757.

[42] C. Lemieux, Monte Carlo and Quasi-Monte Carlo Sampling, Springer Science & Business Media, 2009. doi:10.1007/978-0-387-78165-5. arXiv:arXiv:1011.1669v3.

[43] R. Siegel, Transient radiative cooling of a droplet-filled layer, Journal of Heat Transfer 109 (1987) 159–164.

[44] K. C. Smyth, C. R. Shaddix, The elusive history of m = 1.57 - 0.56i for the refractive index of soot, Combustion and Flame 107 (1996) 314–320.

[45] H. Chang, T. T. Charalampopoulos, Determination of the Wavelength Dependence of Refractive Indices of Flame Soot, Proceedings of the Royal Society A: Mathematical, Physical and Engineering Sciences 430 (1990) 577–591.

[46] P. Rodrigues, B. Franzelli, R. Vicquelin, O. Gicquel, N. Darabiha, Coupling an LES approach and a soot sectional model for the study of sooting turbulent non-premixed flames, Combustion and Flame 190 (2018) 477–499.

[47] S. Salenbauch, A. Cuoci, A. Frassoldati, C. Saggese, T. Faravelli, C. Hasse, Modeling soot formation in premixed flames using an Extended Conditional Quadrature Method of Moments, Combustion and Flame 162 (2015) 2529 – 2543.

[48] M. E. Mueller, G. Blanquart, H. Pitsch, Hybrid Method of Moments for modeling soot formation and growth, Combustion and Flame 156 (2009) 1143 – 1155.

[49] U. O. Köylü, G. M. Faeth, Optical properties of soot in buoyant laminar diffusion flames, Journal of Heat Transfer 116 (1994) 971–979.

[50] T. L. Farias, Ü. Ö. Köylü, M. G. Carvalho, Range of validity of the RayleighDebyeGans theory for optics of fractal aggregates, Applied Optics (1996).

[51] J. Yon, F. Liu, J. Morán, A. Fuentes, Impact of the primary particle polydispersity on the radiative properties of soot aggregates, Proceedings of the Combustion Institute 37 (2019) 1151–1159.

[52] C. M. Sorensen, Light scattering by fractal aggregates: A review, Aerosol Science and Technology 35 (2001) 648–687.

[53] D. W. Weinert, T. G. Cleary, G. W. Mulholland, P. F. Beever, Light scattering characteristics and size distribution of smoke and nuisance aerosols, Fire Safety Science (2003) 209–220.

[54] V. Eymet, A. M. Brasil, M. El Hafi, T. L. Farias, P. J. Coelho, Numerical investigation of the effect of soot aggregation on the radiative properties in the infrared region and radiative heat transfer, Journal of Quantitative Spectroscopy and Radiative Transfer 74 (2002) 697–718.

[55] W. H. Dalzell, A. F. Sarofim, Optical constants of soot and their application to heat-flux calculations, Journal of Heat Transfer 91 (1969) 100–104.

Conflict of interest

« A Quasi-Monte Carlo method to compute scattering effects in radiative heat transfer: application to a sooted jet flame »

We certify that we have NO affiliations with or involvement in any organization or entity with any financial interest or non-financial interest in the subject matter or materials discussed in this manuscript.

Kevin Torres Monclard, Olivier Gicquel, Ronan Vicquelin